ARTICLE OPEN

Superconducting circuit protected by two-Cooper-pair tunneling

W. C. Smith[1,2]*, A. Kou[1], X. Xiao[1], U. Vool[1] and M. H. Devoret[1]*

We present a protected superconducting qubit based on an effective circuit element that only allows pairs of Cooper pairs to tunnel. These dynamics give rise to a nearly degenerate ground state manifold indexed by the parity of tunneled Cooper pairs. We show that, when the circuit element is shunted by a large capacitance, this manifold can be used as a logical qubit that we expect to be insensitive to multiple relaxation and dephasing mechanisms.

INTRODUCTION

Superconducting circuits are widely recognized as a powerful potential platform for quantum computation and now stand at the frontier of quantum error correction.[1] Future progress will likely stem from two complementary strategies: (i) active error correction characterized by measurement-based[2–4] and autonomous[5–8] stabilization, and (ii) passive error correction characterized by protected qubits,[9] and references therein]. We address strategy (ii) in this article by designing an experimentally accessible protected qubit.

The transmon qubit[10] has proven to be a remarkably successful prototype of a protected qubit. Its circuit (depicted in Fig. 1a) contains a Josephson junction whose potential energy is $U = -E_J \cos \varphi$, with E_J being the tunneling energy and φ being the superconducting phase across the junction. The large shunt capacitance imposes a large effective mass for the analogous "particle in a box," confining the low-energy wavefunctions near $\varphi = 0$, the only minimum for $\varphi \in (-\pi, \pi)$. This confinement suppresses the susceptibility of the qubit to offset charge noise and renders the energy spectrum approximately harmonic with level spacing much smaller than E_J (see Fig. 1b). On the other hand, circuit elements with degenerate phase states that only allow tunneling of pairs of Cooper pairs, meaning their potential energy is $U = -E_J \cos 2\varphi$, have been developed in recent years as a building block for topologically protected qubits.[11,12] In this article, we propose a transmon-like qubit with additional protection from environmental noise by combining the large shunt capacitance of the transmon with such a $\cos 2\varphi$ circuit element (the cross-hatched box in Fig. 1c). In this case, the wavefunctions are localized near $\varphi = 0, \pi$ (see Fig. 1d), resulting in a nearly degenerate harmonic level arrangement. While the detrimental effects of offset charge noise are similarly suppressed in this circuit, sensitivity of the qubit to other decoherence mechanisms is also reduced, owing to the conservation of Cooper pair number parity.

In this article, we introduce a few-body transmon-type qubit where the charge carriers are exclusively pairs of Cooper pairs. Our central result is that there exists an experimentally attainable parameter regime for which conservative predictions of relaxation and dephasing times exceed 1 ms, i.e., an order of magnitude higher than those of typical transmons, given the same environmental noise.[13,14] In the following section, we describe a toy model for the protected qubit. We proceed by analytically and numerically examining the Hamiltonian for the full superconducting circuit. Our attention then turns to properties of the ground state manifold, which we envision using as a protected qubit. A brief discussion about the concept of protection and examples of protected qubits, as well as our perspectives on readout and control, follows.

RESULTS

cos 2φ element

We first examine the advantages of the ideal circuit in Fig. 1c as a protected qubit. This circuit can be viewed as a Josephson-junction-like element (the cross-hatched box) shunted by a capacitance. Pairs of Cooper pairs are the only charge excitations permitted to tunnel through this element.[11] In the Cooper pair number basis, the potential energy assumes the form

$$-\frac{1}{2}E_J \sum_{N=-\infty}^{\infty} (|N\rangle\langle N+2| + |N+2\rangle\langle N|) = -E_J \cos 2\varphi, \quad (1)$$

where E_J is the effective tunneling energy of the process. This expression follows from the conjugacy relation $[\varphi, N] = i$, where N is the number of Cooper pairs that have tunneled. The invariance of the potential under translations in φ by multiples of π implies that half-fluxons are able to traverse the element.

The shunt capacitance and other charging effects produce a quadratic kinetic energy, yielding the Hamiltonian

$$H = 4E_C(N - N_g)^2 - E_J \cos 2\varphi, \quad (2)$$

where E_C is the charging energy and N_g is the offset charge. This offset charge has been introduced due to the periodicity of the Hamiltonian in φ, which reflects the presence of a superconducting island in the circuit (as colored in Fig. 1c).

Since the circuit element only allows pairs of Cooper pairs to tunnel, the parity of the number of Cooper pairs that have tunneled is preserved under the action of the Hamiltonian. This property leads to two nearly degenerate ground states $|+\rangle$ and $|-\rangle$, which only consist of even and odd Cooper pair number states, respectively.[12] Since these states have no overlap in charge space (equivalently, they have opposite periodicity in phase space —see Fig. 1d), we have $\langle -|\mathcal{O}|+\rangle \approx 0$ for any sufficiently local

[1]Departments of Applied Physics and Physics, Yale University, New Haven, CT 06520, USA; [2]Present address: QUANTIC Team, INRIA Paris, 2 rue Simone Iff, 75012 Paris, France.
*email: william.smith@inria.fr; michel.devoret@yale.edu
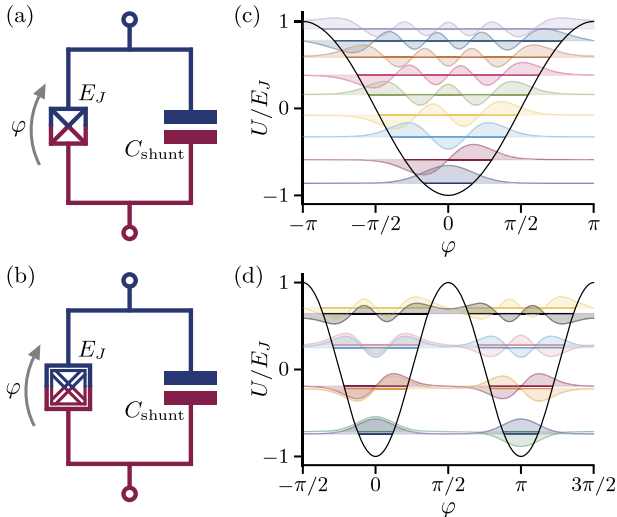
Fig. 1 Principle of the protected qubit. a Electrical circuit for the transmon qubit. **b** Potential energy of the transmon with energy levels and wavefunctions for the first few eigenstates. **c** Electrical circuit for the idealized protected qubit. The cross-hatched circuit element comprises a capacitance in parallel with an inductive element that exclusively permits the tunneling of pairs of Cooper pairs. The superconducting island is indicated by color. **d** Potential energy of the ideal charge-protected qubit with the lowest-energy levels and wavefunctions.

operator $\mathcal{O}$. Furthermore, the states $|\circlearrowleft/\circlearrowright\rangle = \frac{1}{\sqrt{2}}(|+\rangle \pm |-\rangle)$ are, respectively, localized near $\varphi = 0, \pi$ (see Fig. 1d). As these states have suppressed overlap in phase space for large E_J/E_C (i.e., they are roughly inversely periodic in charge space), we have $\langle\circlearrowright|\mathcal{O}|\circlearrowleft\rangle \approx 0$ for similarly local $\mathcal{O}$. These are precisely the conditions for simultaneously suppressing spurious transitions and phase changes between the states[15] [resembling a Gottesman–Kitaev–Preskill (GKP) encoding on a circle[16]].

More concretely, the ground state splitting obeys

$$\Delta E \approx 16 E_C \sqrt{\frac{2}{\pi}} \left(\frac{2E_J}{E_C}\right)^{3/4} e^{-\sqrt{2E_J/E_C}} \cos(\pi N_g), \tag{3}$$

for large E_J/E_C (see Supplementary information). The two ground state energies oscillate out of phase with one another in N_g. Moreover, this shows that the splitting, as well as the charge dispersion, is exponentially suppressed in E_J/E_C. Thus, the role of the shunt capacitance is to decrease the charging energy E_C and hence mitigate offset charge noise, much like in the transmon qubit.[10]

Superconducting circuit

We now detail the superconducting circuit necessary to practically implement the sought-after $\cos 2\varphi$ Josephson element. This circuit, depicted in Fig. 2a, is composed of two identical arms, each containing a Josephson junction in series with super-inductances,[17,18] arranged in parallel[19,20] and shunted by a large capacitance. These superinductances are split in half and placed on either side of the respective Josephson junctions to avoid large capacitances to ground. Kirchoff's current law allows us to treat the phases across the superinductances in series as equal. When the external magnetic flux threading the inductive loop reaches half of a flux quantum, i.e., when $\varphi_{ext} = \pi$, the loop approximates the cross-hatched box in Fig. 1c. At this particular bias point, a Cooper pair can only tunnel through one of the Josephson junctions if it is accompanied by another Cooper pair tunneling through the other junction (in either direction). Conversely, a
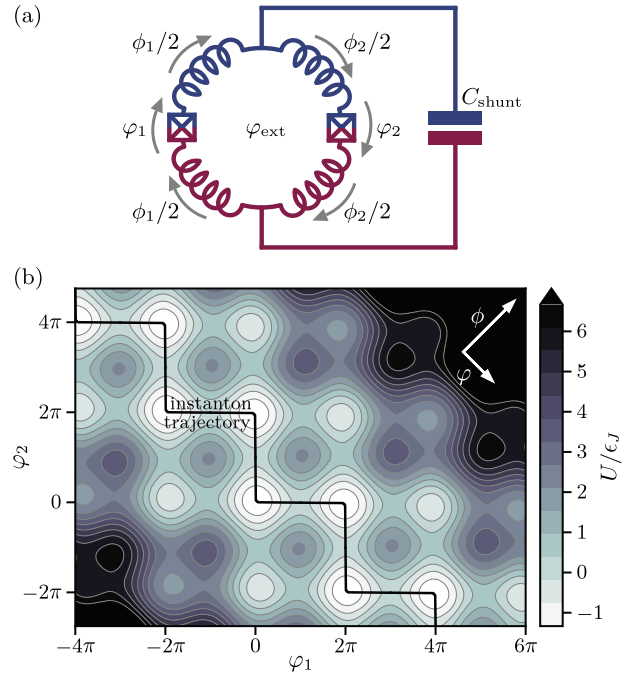
Fig. 2 Physical realization of the cos 2φ element. a Reduced electrical circuit for the physical protected qubit. When $\varphi_{ext} = \pi$, the two Josephson junctions and superinductances collectively behave as the cross-hatched element. The superconducting island is indicated by color. **b** Contour plot of the potential energy U in Eq. (5) in the $\varphi_1\varphi_2$-plane at $\varphi_{ext} = \pi$ for $\theta = 0$. The numerically computed instanton trajectory between adjacent potential minima is overlaid in black. Importantly, this trajectory closely resembles a sequence of straight lines.

fluxon traversing a single Josephson junction corresponds to a half-fluxon traversing the whole element.

We consider the symmetric and antisymmetric combinations of superconducting phase coordinates

$$\phi = \varphi_1 + \varphi_2 \qquad \varphi = \frac{1}{2}(\varphi_1 - \varphi_2) \qquad \theta = \frac{1}{2}(\phi_1 - \phi_2), \tag{4}$$

and their conjugate charges $\{n, N, \eta\}$ in numbers of Cooper pairs. Note that the prefactor in the definition of φ is chosen to bring the coordinate into agreement with the phase drop across the inductive loop in the limit that θ vanishes. The Hamiltonian reads

$$H = 4\epsilon_C \left[2n^2 + \tfrac{1}{2}(N - N_g - \eta)^2 + x\eta^2\right] \\ + \epsilon_L \left[\tfrac{1}{4}(\phi - \varphi_{ext})^2 + \theta^2\right] - 2\epsilon_J \cos\varphi \cos\tfrac{\phi}{2}, \tag{5}$$

where ϵ_C and ϵ_J are the single junction charging and tunneling energies, $2\epsilon_L$ is the inductive energy of each superinductance, $x \equiv C_J/C_{shunt}$ is the ratio of the junction capacitance to the shunt capacitance, and N_g is the offset charge on the superconducting island (see Fig. 2a).

From this expression, it is clear that this circuit has three strongly coupled modes. The ϕ mode is flux-dependent and is strongly and nonlinearly coupled, via the Josephson junctions, to the φ mode. The φ mode is offset charge dependent and strongly but linearly capacitively coupled to the θ mode. Our analysis and the effects observed in the remainder of this article require the parameter regime $\epsilon_L \ll \epsilon_J$, $\epsilon_C \lesssim \epsilon_J$, and $x \ll 1$ (Specifically, the semiclassical theory breaks down at $\epsilon_L \sim \epsilon_J$ and the protection breaks down for $x \gtrsim 0.1$). In particular, the parameters chosen for numerical simulations are $\epsilon_J/h = 15$ GHz, $\epsilon_C/h = 2$ GHz, $\epsilon_L/h = 1$ GHz, and $x = 0.02$—which are similar to those of recent fluxonium devices.[17,21]
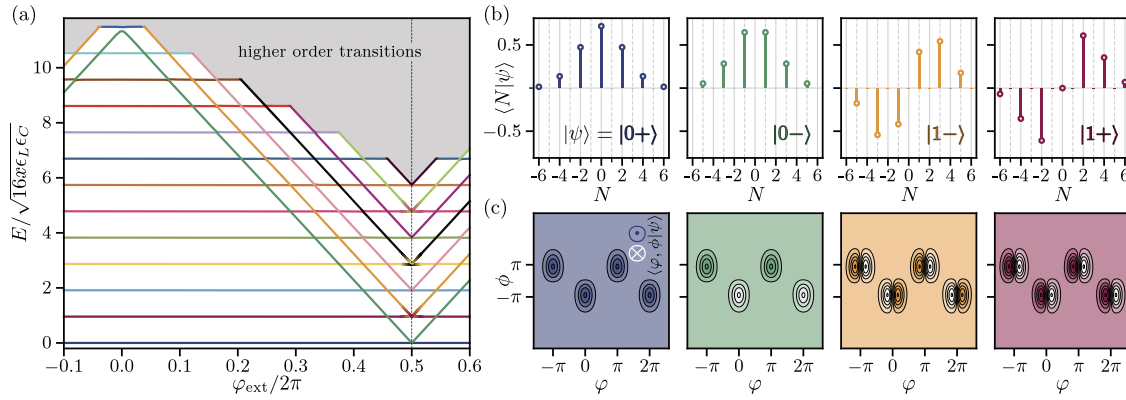
Fig. 3 Energy levels and wavefunctions. a Normalized transition energies E from the ground state of the Hamiltonian in Eq. (5) as a function of external flux at $N_g = 0$. The essential feature is the presence of a flux-independent plasmon mode (maroon) with energy $\sqrt{16x\epsilon_L\epsilon_C}$ and a flux-dependent fluxon mode (green). The coloring reflects the assigned quantum numbers. **b** Charge wavefunctions $\langle N|\psi\rangle = \langle N|m\pm\rangle$ of the first four eigenstates of Eq. (5), illustrating that the plasmon excitation index $m = 0, 1, \ldots$ indicates the functional form while the fluxon excitation index $\pm$ indicates charge parity. **c** Phase wavefunctions $\langle\varphi, \phi|\psi\rangle$ of the first four eigenstates of Eq. (5), showing that the intrawell excitation number corresponds to the plasmon index and that the bonding/antibonding configuration corresponds to the fluxon index. All wavefunctions are computed at $\varphi_{ext} = \pi$.

Semiclassical theory

In order to gain insight into the structure of the Hamiltonian in Eq. (5), we briefly revisit its potential energy U in the $\varphi_1\varphi_2$-plane, which is plotted in Fig. 2b for $\theta = 0$. The cosine terms in the potential form a two-dimensional "egg carton" of wells. The minimum of the quadratic term in the potential occurs at $\varphi_1 + \varphi_2 = \varphi_{ext}$, which generally falls between adjacent diagonal ridges of cosine wells. At the special value of $\varphi_{ext} = \pi$, these two ridges are degenerate. Near this value of the external flux, we consider the path of the system between neighboring potential minima by numerically solving for the three-dimensional instanton[22] trajectory (see Supplementary information).

We then constrain the system to this maximally probable tunneling path. For the parameters mentioned above, this path is well-described by

$$\phi = \frac{1}{1+z}\left(2\left|\varphi - 2\pi \text{ round } \frac{\varphi}{2\pi}\right| + z\varphi_{ext}\right), \quad (6)$$

where $z \equiv \epsilon_L/\epsilon_J$ is a small parameter. Plugging this expression into the Hamiltonian in Eq. (5), approximating the resulting one-dimensional potential by the first few terms in its Fourier series, and Taylor expanding about $z = 0$ yields $H \approx H_{eff}$ with

$$\begin{aligned} H_{eff} = \quad & 4\epsilon_C\left[\frac{1}{4(1-z)}(N - N_g - \eta)^2 + x\eta^2\right] + \epsilon_L\theta^2 \\ & - \frac{16}{3\pi}\epsilon_L(\pi - \phi_{ext})\cos\varphi - \epsilon_J\left(1 - \frac{5}{4}z\right)\cos 2\varphi \end{aligned} \quad (7)$$

to leading order. Here, $\phi_{ext} = \left|\varphi_{ext} - 4\pi \text{ round } \frac{\varphi_{ext}}{4\pi}\right|$ and we have discarded terms higher than the second harmonic or $O(\epsilon_L)$ (see Supplementary information for additional terms). This treatment exposes the "$\cos 2\varphi$ nature" of the potential at $\varphi_{ext} = \pi$, where the $\cos\varphi$ term vanishes. By comparison to Eq. (2), we see that the added complication is that the φ mode is strongly coupled to the θ mode. The resulting hybridization is a central ingredient to understanding properties of the system beyond the ground state manifold (see Wavefunctions).

We comment that this approximation neglects quantum fluctuations that are perpendicular to the path in Eq. (6). This is consequently a semiclassical approximation: we have minimized the energy of the system with respect to the dynamical coordinate orthogonal to the trajectory.[22] Moreover, from Fig. 2b, it is clear that the approximation we have made is that fluxons traverse a single Josephson junction at a time.

Energy spectrum

From numerical diagonalization of Eq. (5) (see Supplementary information), we obtain the dependence of the energy levels on external flux as shown in Fig. 3a.[23] At $\varphi_{ext} = \pi$ (the dashed line in Fig. 3a), the spectrum resembles a doubled harmonic oscillator with energy $\sqrt{16x\epsilon_L\epsilon_C}$. Once φ_{ext} deviates from π, half of the energy levels increase in energy linearly with slope $\sim \frac{32}{3}\epsilon_L$. The other half of the energy levels form a flux-independent harmonic ladder.

We can understand this level structure as that of two emergent modes (see also Supplementary information). The first mode is flux-dependent and its excitations correspond to the number of magnetic flux vortices, or fluxons, enclosed by the inductive loop in Fig. 2a. In turn, the number of enclosed fluxons identically maps onto the magnitude and chirality of the circulating persistent current in the inductive loop. The second mode is flux-independent and its excitations correspond to quantized charge density oscillations, or plasmons, across the inductive loop/shunt capacitance in Fig. 2a. Each plasmon involves the two super-inductances (energy $2\epsilon_L$ in parallel) and the shunt capacitance (energy $x\epsilon_C$), and hence has energy $\sqrt{16x\epsilon_L\epsilon_C}$. Hereafter, we refer to these modes as the "fluxon mode" and the "plasmon mode," respectively. Additionally, we assign the labels $|m\bullet\rangle$ to the lowest-energy states, where m denotes the number of plasmons and $\bullet$ (or $\circ$) denotes the presence (or absence) of a fluxon excitation relative to the ground state (Here, we restrict the Hilbert space to the two fluxon states with lowest-energy). Note that the fluxon place-holder indices are defined by

$$\bullet/\circ = \begin{cases} \circlearrowleft/\circlearrowleft, & \text{for } \varphi_{ext} \text{ mod } 2\pi < \pi \\ -/+, & \text{for } \varphi_{ext} \text{ mod } 2\pi = \pi, \\ \circlearrowright/\circlearrowright, & \text{for } \varphi_{ext} \text{ mod } 2\pi > \pi \end{cases} \quad (8)$$

where $|m\pm\rangle = |m\rangle \otimes \frac{1}{\sqrt{2}}(|\circlearrowleft\rangle \pm |\circlearrowright\rangle)$ and the index $|\circlearrowleft/\circlearrowright\rangle$ represents the persistent current direction. This labeling serves the purpose of assigning quantum numbers consistently for all external flux values (see the colors in Fig. 3a — note that the coloring changes for only the odd-numbered plasmon states, due to the fact that the eigenstate with even overall parity has lower energy for each plasmon state, and that the overall parity includes both a plasmon and a fluxon component), except the particular case $\varphi_{ext} \text{ mod } 2\pi = 0$ that we do not focus on.

Wavefunctions

Calculated charge wavefunctions $\langle N|\psi\rangle$ and phase wavefunctions $\langle\varphi,\phi|\psi\rangle$, obtained from numerical diagonalization of Eq. (5), are shown in Figs. 3b, c for the four lowest-energy eigenstates at $\varphi_{\text{ext}} = \pi$. Roughly, the phase wavefunctions are computed by projection of the θ coordinate and a Fourier transform to the $\varphi\phi$-plane, while the charge wavefunctions are computed by projection of the θ coordinate and constraint to the trajectory in Eq. (6) (see Supplementary information for details).

The charge wavefunctions are grid states with Fock-state envelopes.[16,24] For fluxon excitation index $+/-$, these grid states are superpositions of even/odd Cooper pair number states. Additionally, m corresponds to the order of the Fock-state envelope. Note that a logical qubit encoded in $|0+\rangle$ and $|0-\rangle$ is protected from spurious transitions except those mediated by operators that flip Cooper pair parity.

On the other hand, the phase wavefunctions are approximately Fock states localized within the potential energy wells (see Fig. 2b).[21] The fluxon index $+/-$ denotes whether the state $|m\pm\rangle$ is a symmetric (bonding) or antisymmetric (antibonding) superposition of states localized within opposite ridges of potential wells. These ridges correspond to persistent currents of opposite chirality, and hence also to the absence/presence of a fluxon in the inductive loop of the circuit.[25] In this picture, m refers to the Fock order of the localized states. Finally, operators that flip Cooper pair parity correspond to odd functions of ϕ or functions of φ with period an odd division of 2π, which can be seen from Fig. 3c to mediate the transition $|m+\rangle \leftrightarrow |m-\rangle$.

Matrix elements

In the previous sections, we analyzed the multi-mode Hamiltonian describing the superconducting circuit in Fig. 2a. Numerical diagonalization of this Hamiltonian showed the emergence of a linear plasmon mode and a nonlinear fluxon mode. In the following sections, we consider the properties of the logical qubit formed by $\{|0+\rangle,|0-\rangle\}$, the two lowest-energy eigenstates at $\varphi_{\text{ext}} = \pi$, which generalizes to $\{|0\circ\rangle,|0\bullet\rangle\}$ away from $\varphi_{\text{ext}} = \pi$.

To better elucidate which types of operators can and cannot induce transitions between the two states of the qubit, we examine the relevant matrix elements corresponding to capacitive and inductive coupling. This discussion is particularly relevant to understanding the expected dominant loss mechanisms and designing a measurement and control apparatus that does not directly couple to the qubit.

For capacitive coupling, a generic voltage V couples to the superconducting island of the circuit in Fig. 2a via a gate capacitance C_g and will append the term

$$H_{\text{int}} = \frac{C_g}{C_{\text{shunt}} + C_g}(2e\eta)V \tag{9}$$

to the Hamiltonian in Eq. (5), in addition to dressing the shunt capacitance. This voltage may be a degree of freedom of another mode in the embedding circuit, a noise source, or an ac drive. We therefore see that the susceptibility of undergoing a transition from the ground state, due to capacitive coupling to the qubit island, is directly related to the matrix element $\langle\psi|\eta|0\circ\rangle$.

For inductive coupling, a generic current I couples to the circuit via a small inductance L_s shared with the inductive loop, which adds the term

$$H_{\text{int}} = \frac{L_s}{2L}(\phi_0\phi)I \tag{10}$$

to the Hamiltonian in Eq. (5). Here, $\phi_0 = \hbar/2e$ is the reduced magnetic flux quantum and L is the superinductance in each arm of the qubit (i.e., $\epsilon_L = \phi_0^2/L$). Like the voltage source, this current may represent an internal or environmental degree of freedom. We see that the susceptibility of undergoing a transition from the ground state, due to inductive coupling to the inductive loop, is related to the matrix element $\langle\psi|\phi|0\circ\rangle$.

Limiting the Hilbert space to the six lowest-energy eigenstates $\{|m\pm\rangle : m = 0,1,2\}$, we numerically compute the normalized matrix elements

$$|\mathcal{O}_\psi|^2 \equiv \frac{|\langle\psi|\mathcal{O}|0\circ\rangle|^2}{\langle0\circ|\mathcal{O}^\dagger\mathcal{O}|0\circ\rangle} \tag{11}$$

from the ground state $|0\circ\rangle$ for the operators $\mathcal{O} = \eta,\phi$. Results are plotted in Fig. 4. Note that $\sum_\psi|\mathcal{O}_\psi|^2 = 1$ and $|\mathcal{O}_\psi|^2 > 0$, so we may reasonably consider these as transition probabilities via $\mathcal{O}$.

We see from Fig. 4a that transitions mediated by capacitive coupling to the qubit island are only allowed from $|0\circ\rangle$ to $|1\circ\rangle$. These selection rules result from the decoupling of the even and odd Cooper pair number parity manifolds (see Supplementary information). Most importantly, transitions between qubit states are forbidden, meaning capacitive coupling offers a promising ingredient for indirect qubit measurement and control (see Discussion). Conversely, inductive coupling to the inductive loop of the qubit permits transitions between $|0\circ\rangle$ and $|0\bullet\rangle$ in the vicinity of $\varphi_{\text{ext}} = \pi$, as shown in Fig. 4b. This effect arises because the operator ϕ induces transitions between the Cooper pair parity manifolds, as can be seen from the Fourier series for Eq. (6). As a consequence, we expect that relaxation of the qubit will be primarily due to inductive loss in the superinductances (see Relaxation).

Disorder

A highly symmetric superconducting circuit is usually fragile in view of unavoidable fabrication imperfections.[25] The symmetry of our circuit involving the two inductive arms in Fig. 2a may be broken in three parameters: the Josephson energies of the junctions, the capacitances of the junctions, or the superinductances. To analyze these effects, we numerically diagonalize Eq. (5) and examine the energy splitting ΔE (evaluated at $N_g = 0$), as well as the charge dispersion $\epsilon = \max_{N_g}\Delta E - \min_{N_g}\Delta E$ of the $\{|0+\rangle,|0-\rangle\}$ manifold at $\varphi_{\text{ext}} = \pi$. A dimensionless quantity $\delta \in [0,1)$ is introduced to parameterize the extent of asymmetry in all three cases, and the δ-dependence of the energies ΔE and ϵ is studied.

We model disorder in the Josephson energies of the junctions by allowing the values of ϵ_J to deviate. We, therefore, set the left and right junction tunneling energies to $(1\pm\delta_J)\epsilon_J$, respectively, where δ_J is the aforementioned asymmetry parameter. The Hamiltonian in Eq. (5) is perturbed by the term

$$H' = 2\epsilon_J\delta_J\sin\varphi\sin\frac{\phi}{2}. \tag{12}$$

See Fig. 5 for a plot of ΔE and ϵ as a function of δ_J. The important feature in these plots is that the charge dispersion decreases exponentially while the splitting increases exponentially with δ_J (The extrapolation of the charge dispersion as a function of the disorder beyond $\delta = 0.6$ is due to numerical instabilities inherent to low-energy quantities paired with disappearance of an efficient diagonalization basis for large disorder). These features arise from the effective Hamiltonian in Eq. (7) being accompanied by 2π-periodic terms in the presence of disorder. In this case of disorder in ϵ_J, the semiclassical approximations used earlier lead to $H' \approx H'_{\text{eff}}$ with

$$H'_{\text{eff}} = -\frac{16}{3\pi}\epsilon_J\delta_J\left(\sin\varphi - \frac{1}{5}\sin 3\varphi\right), \tag{13}$$

which evidently permits the tunneling of single Cooper pairs across the element. The resulting qubit retains characteristics of the symmetric circuit, as well as the asymmetric/transmon-like circuit.
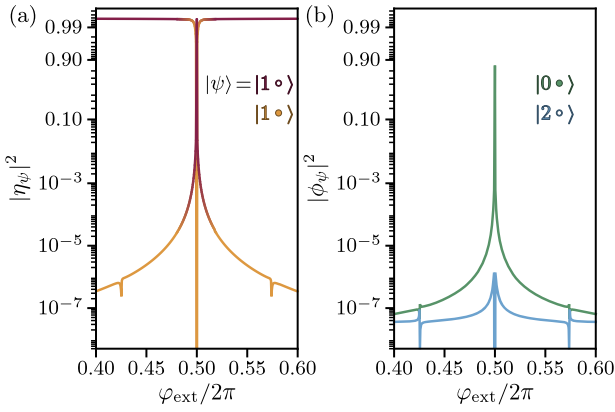
Fig. 4 Selection rules. a Normalized charge matrix elements $|\eta_\psi|^2$ between the ground state $|0\circ\rangle$ and the excited state $|\psi\rangle$, showing immunity of the qubit manifold to capacitive coupling. **b** Normalized phase matrix elements $|\phi_\psi|^2$ between states $|0\circ\rangle$ and $|\psi\rangle$. This matrix element is near-unity between the two qubit states at $\varphi_{\text{ext}} = \pi$, meaning the qubit manifold is primarily susceptible to inductive loss.

Analogously, we set the left and right junction charging energies to $\epsilon_C/(1 \pm \delta_C)$, respectively. Aside from dressing the charging energy, the Hamiltonian in Eq. (5) inherits the term

$$H' = -8\epsilon_C \frac{\delta_C}{1 - \delta_C^2} n(N - N_{\text{g}} - \eta), \tag{14}$$

whose effect on the qubit manifold is plotted in Fig. 5.

This form for capacitive disorder is assumed due to the fact that, if $\delta_J = \delta_C \equiv \delta_A$, then the product $\epsilon_J \epsilon_C$ is kept constant for both junctions under the effects of disorder. This corresponds to the physical case where the junction plasma frequencies are fixed by oxidation, but their areas differ due to fabrication imperfections. Here, the junction areas are $(1 \pm \delta_A)A$ because $A \propto \sqrt{\epsilon_J/\epsilon_C}$. The consequences of area disorder are plotted in Fig. 5.

Following the same procedure, we set the left and right superinductance inductive energies to $\epsilon_L/(1 \pm \delta_L)$, respectively. This form is taken in order to fix the total linear inductance in the loop. Aside from dressing the inductive energy, the Hamiltonian in Eq. (5) is perturbed by

$$H' = \epsilon_L \frac{\delta_L}{1 - \delta_L^2}(\phi - \varphi_{\text{ext}})\theta. \tag{15}$$
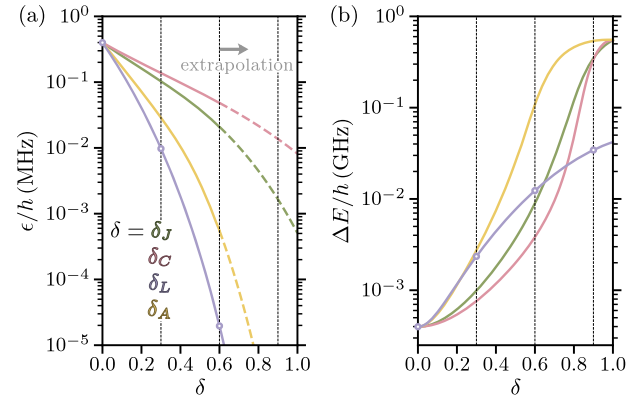
Note in Fig. 5 that the charge dispersion and energy splitting follow the same general trend for inductive disorder as for the other three. The key difference is that the charge dispersion decreases more quickly than for any other form of disorder. Oppositely, the splitting is initially the same as for area disorder, but the slope decreases in δ_L. We conclude that disorder allows us to engineer a circuit with a sufficiently non-degenerate ground state manifold whose charge dispersion is largely suppressed. For reasons that will become clear in two sections, these features are extremely valuable for designing a qubit that is protected from dephasing.

Relaxation

We model loss due to an arbitrary channel using Fermi's Golden Rule. This gives us the relaxation rate, including both emission and absorption, of

$$\frac{1}{T_1} = \frac{1}{\hbar^2}|\langle 0 + |\mathcal{O}|0-\rangle|^2[S_{\mathcal{E}\mathcal{E}}(\Delta\omega) + S_{\mathcal{E}\mathcal{E}}(-\Delta\omega)]. \tag{16}$$

In this expression, $\mathcal{O}$ is the operator of the circuit coupling to a noisy bath variable $\mathcal{E}(t)$, the noise spectral density of which is

given by $S_{\mathcal{E}\mathcal{E}}(\omega)$. Note that $\Delta E = \hbar \Delta\omega$. In this section, we calculate the relaxation rates for the expected dominant loss mechanisms of the qubit based on numerical diagonalization of the full Hamiltonian in Eq. (5). We perform this calculation for various degrees of inductive disorder δ_L (see Fig. 5).

We consider four possible loss channels for the qubit: capacitive loss, inductive loss, Purcell loss, and quasiparticle tunneling.[26] Capacitive loss involves dielectric dissipation in the Josephson junction capacitances. In this case, we have $\mathcal{O} = 2eN_i = 2e[n \pm \frac{1}{2}(N - \eta)]$ for the charge across the i-th junction and $\mathcal{E} = V$ for a bath voltage with

$$S_{VV}(\omega) + S_{VV}(-\omega) = \frac{2\hbar}{C_J \mathcal{Q}_{\text{cap}}(\omega)} \coth\frac{\hbar|\omega|}{2k_B T}. \tag{17}$$

Here, $C_J = e^2/2\epsilon_C$ is the junction capacitance, T is the temperature, and $\mathcal{Q}_{\text{cap}}(\omega)$ is a frequency-dependent quality factor[27] with nominal value $Q_{\text{cap}} \sim 1 \times 10^6$[28] (see Supplementary information for more details).

Depending on the specific implementation, inductive loss may occur within the superinductances via quasiparticle tunneling.[26] This situation can be modeled by taking $\mathcal{O} = \phi_0 \phi_i$ for the flux across the i-th superinductance and $\mathcal{E} = I$ for a bath current with

$$S_{II}(\omega) + S_{II}(-\omega) = \frac{2\hbar}{L_i \mathcal{Q}_{\text{ind}}(\omega)} \coth\frac{\hbar|\omega|}{2k_B T}. \tag{18}$$

In this expression, $L_i = (1 \pm \delta_L)L$ is the i-th superinductance and $\mathcal{Q}_{\text{ind}}(\omega)$ is a frequency-dependent quality factor with nominal value $Q_{\text{ind}} \sim 500 \times 10^6$.[26] As shown in the Supplementary information, this frequency dependence is included to extrapolate to small qubit transition frequencies.

Loss due to the Purcell effect should mainly arise from coupling of the qubit to the plasmon mode, which we model as dielectric loss in the shunt capacitance. As such, we have $\mathcal{O} = 2e\eta$ and $\mathcal{E} = V$ for a bath voltage with the same noise spectral density as Eq. (17), but with C_J replaced by C_{shunt}.

Finally, quasiparticle tunneling is expected to occur across either Josephson junction and contribute to qubit relaxation.[26] In this case, we have $\mathcal{O} = 2\phi_0 \sin\frac{\varphi_i}{2}$ for the i-th junction and the noise spectral density

$$S_{\text{qp}}(\omega) + S_{\text{qp}}(-\omega) = 2\hbar\omega \operatorname{Re} Y_{\text{qp}}(\omega) \coth\frac{\hbar\omega}{2k_B T}, \tag{19}$$

with $\operatorname{Re} Y_{\text{qp}}(\omega)$ being the dissipative part of the Josephson junction admittance[29] (see Supplementary information for the

Fig. 5 Effects of disorder. a Plot of the charge dispersion ϵ of the qubit transition as a function of disorder parameters δ. Here, δ_J, δ_C, and δ_L correspond to disorder in the characteristic energy scales ϵ_J, ϵ_C, and ϵ_L, respectively. Disorder in the area of the two Josephson junctions is represented by δ_A. **b** Plot of the energy splitting ΔE as a function of disorder parameters δ. The dashed lines and circles indicate the values of δ_L used for inductive disorder when computing coherence estimates.

Table 1. Expected relaxation times T_1 and pure dephasing times T_ϕ at $\varphi_{\text{ext}} = \pi$ through various channels.

Coherence time estimates						
Loss channel	$\mathcal{O}$	Quality factor	T_1 (ms)			
			$\delta_L = 0.0$	$\delta_L = 0.3$	$\delta_L = 0.6$	$\delta_L = 0.9$
Capacitive	$2eN_i$	$Q_{\text{cap}} \sim 1 \times 10^{6}$[28]	780 000	17 000	1 000	18
Inductive	$\phi_0 \phi_i$	$Q_{\text{ind}} \sim 500 \times 10^{6}$[26]	0.61	0.79	1.1	1.4
Purcell	$2e\eta$	$Q_{\text{cap}} \sim 1 \times 10^{6}$[28]	∞	2 500	380	470
Quasiparticle	$2\phi_0 \sin \frac{\varphi_i}{2}$	$1/x_{\text{qp}}^* \sim 0.3 \times 10^{6}$[26]	∞	∞	∞	∞
Dephasing channel	λ	Spectral density amplitude	T_ϕ (ms)			
			$\delta_L = 0.0$	$\delta_L = 0.3$	$\delta_L = 0.6$	$\delta_L = 0.9$
Charge	N_g	$\sqrt{A_{N_g}}^* \sim 1 \times 10^{-4}$[54]	0.0037	0.15	74	3.3×10^6
Flux	φ_{ext}	$\sqrt{A_{\varphi_{\text{ext}}}}/2\pi \sim 3 \times 10^{-6}$[34]	0.022	0.13	0.67	1.8
Shot	n_p	$n_{\text{th}}/Q_{\text{cap}} \sim 1 \times 10^{-7}$[28]	4.6	4.8	5.3	8.7
Critical current	ϵ_J	$\sqrt{A_{\epsilon_J}}/\epsilon_J \sim 5 \times 10^{-7}$[36]	210	40	8.2	2.9

The operators $\mathcal{O}$ coupling to the bath and the noisy parameters λ are listed in addition to the associated quality factors and spectral density amplitudes, respectively. Relaxation and dephasing times are shown for varying cases of inductive disorder: $\delta_L = 0.0, 0.3, 0.6, 0.9$ (see also Fig. 5). The operators N_i depict the number of Cooper pairs having tunneled across the two Josephson junctions, i.e., $N_i = n \pm \frac{1}{2}(N - \eta)$. Entries that read "$\infty$" represent numerical infinity. *These values are reported for clarity, but have no bearing on the estimates shown (see Relaxation, Pure dephasing).

explicit form). Note that this admittance scales linearly in both ϵ_J and the quasiparticle density x_{qp} defined relative to that of Cooper pairs.

The calculated relaxation rates and the corresponding components of Eq. (16) are shown in Table 1 for all four loss channels at $\varphi_{\text{ext}} = \pi$. For both capacitive and inductive loss, we note that measurements have not yet been performed using qubits with extremely small energy splittings, and the calculation presented here relies on an extrapolation to such frequencies. A key feature is the complete absence of quasiparticle loss, as in the fluxonium qubit.[26] Additionally, we see that the asymmetric qubit is marginally less susceptible to inductive loss than the symmetric qubit. This improvement comes at the cost of the susceptibility to capacitive and Purcell loss. However, we emphasize that the lifetimes shown in Table 1 are conservative estimates that demonstrate $T_1 \gtrsim 1$ ms, which is at least competitive with state-of-the-art qubit implementations.[13,24,26,30–32]

Pure dephasing

In this section, we examine the dependence of the qubit transition energy ΔE on various system parameters λ corresponding to different dephasing mechanisms. We estimate the dephasing times due to offset charge noise, external flux-noise, photon shot noise in the plasmon mode, and critical current noise. The noise spectral densities are all assumed to be $1/f$ and hence given by $S_{\lambda\lambda}(\omega) = 2\pi A_\lambda/|\omega|$, where $\sqrt{A_\lambda}$ is the amplitude, with the sole exception of shot noise whose spectral density is assumed to be Lorentzian.

In the case of perfect symmetry, the charge dispersion ϵ is identically mapped to ΔE. As a consequence, resilience to dephasing from offset charge noise demands a high degree of degeneracy, making experimental implementation difficult. Fortunately, this issue can be avoided by introducing inductive disorder into the system (see Disorder). In the slow-varying limit for charge noise, the pure dephasing rate is bounded by

$$\frac{1}{T_\phi} = \frac{\pi}{(2e)^2} \epsilon/\hbar, \tag{20}$$

where e is Euler's number.[10] In Table 1, we see that this yields a strict bound on the decoherence time in the case of perfect

symmetry, which is greatly alleviated in the presence of inductive disorder. Note that this estimate does not explicitly involve $\sqrt{A_{N_g}}$ because the slow-varying limit has been taken where the offset charge assumes a random value for each measurement, but does not fluctuate within a given measurement.

At $\varphi_{\text{ext}} = \pi$, the qubit manifold is only susceptible to external flux-noise to second order. However, one can easily obtain the relation $\partial^2 \Delta E / \partial \varphi_{\text{ext}}^2 \propto 1/\Delta E$ (at $\varphi_{\text{ext}} = \pi$), which shows that insensitivity to flux-noise-induced dephasing requires sufficiently weak degeneracy, at odds with the requirement for resilience to charge noise. Once more, introducing inductive disorder avoids this issue. Neglecting components that depend on details of the implementation, the pure dephasing rate[33] is bounded by

$$\frac{1}{T_\phi} = A_{\varphi_{\text{ext}}} \left| \frac{\partial^2 \Delta E}{\partial \varphi_{\text{ext}}^2} \right|, \tag{21}$$

where $\sqrt{A_{\varphi_{\text{ext}}}}/2\pi \sim 3 \times 10^{-6}$ is the amplitude of the noise spectral density[34,35] for φ_{ext}. As in the case of charge noise, this places a stringent limit on the decoherence time of the qubit in the absence of inductive disorder, as we see in Table 1.

We expect the dominant contribution to dephasing due to thermal photons to arise from coupling to the plasmon mode. This mode has an angular frequency $\omega_p \approx \sqrt{16\chi\epsilon_C\epsilon_L}/\hbar$ and an occupation n_p with mean given by $n_{\text{th}} = 1/(e^{\hbar\omega_p/k_B T} - 1)$. To this end, we place a bound on the pure dephasing time T_ϕ using the expression[13]

$$\frac{1}{T_\phi} = n_{\text{th}}\kappa \frac{\chi^2}{\chi^2 + \kappa^2}, \tag{22}$$

where χ is the dispersive shift of the qubit on the plasmon mode and $\kappa = \omega_p/\mathcal{Q}_{\text{cap}}(\omega_p)$ is the linewidth of the plasmon mode. Note that, as for capacitive loss, we use the frequency-dependent dielectric quality factor $\mathcal{Q}_{\text{cap}}(\omega)$ with nominal value $Q_{\text{cap}} \sim 1 \times 10^6$.[28] In all cases, this form of noise is not expected to limit the decoherence time of the qubit (see Table 1).

The final dephasing mechanism we investigate is critical current noise, or fluctuations in the Josephson energy ϵ_J. As in the case of flux-noise, we discard factors that are sensitive to experimental

details and take the dephasing rate to be bounded by[33]

$$\frac{1}{T_\phi} = \sqrt{A_{\epsilon_J}} \left| \frac{\partial \Delta E}{\partial \epsilon_J} \right|, \tag{23}$$

where $\sqrt{A_{\epsilon_J}} \sim 5 \times 10^{-7} \epsilon_J$ is the amplitude of the noise spectral density[36] for ϵ_J. As in the case of photon shot noise, we do not expect critical current noise to place a strict bound on the decoherence time (see Table 1).

At this point, it is clear that inductive asymmetry constitutes a necessary ingredient in the protection of this qubit. In light of Eq. (15), we attribute this to the resulting hybridization of the ϕ and θ modes, which are not directly coupled in the symmetric case (see Eq. (5)). The fluxon transition between the qubit states inherits some character of the plasmon transition, thereby breaking the correspondence between ϵ and ΔE and reducing the flux matrix element $\langle 0|\phi|0+\rangle$.

DISCUSSION

We have proposed a superconducting circuit whose ground state manifold can be made protected, at the Hamiltonian level, from multiple common sources of noise. Here we describe some of the other strategies for achieving protection. The simplest manifestations involve improving quality factors associated with coupling to different thermal baths[30,37,38] and reducing noise spectral densities for different Hamiltonian parameters.[13,39,40] At a higher level, a popular approach to suppressing qubit relaxation has been to localize wavefunctions in disparate regions of phase space to lessen transition matrix elements.[21,24,26,41] On the other hand, delocalization of the same wavefunctions has been shown to mitigate dephasing effects by reducing qubit sensitivity to Hamiltonian parameters.[10,17,31,42–44] Superconducting circuits with multiple degrees of freedom whose qubit wavefunctions are both localized and delocalized combine both of these approaches. In these circuits, quantum information is diffused among constituent local degrees of freedom, providing protection from local perturbations. The many-body limit promises topological protection,[11,15,19,45] in which global operators are necessary to manipulate logical qubits, but the few-body case described here offers an experimentally realistic approximation.[12,20,24,25,32,35,46] In the following paragraphs, we outline the key differences between our circuit and similar proposals.

The heavy fluxonium,[21,41] in which a conventional fluxonium qubit is shunted by a large capacitance, shares many similar features with the circuit in Fig. 2a. In fact, our circuit roughly reduces to that of the conventional fluxonium in the extremely asymmetric limit of $\delta_L \to 1$, and the eigenstates of both circuits are similarly represented in terms of persistent currents. The two main differences are that our circuit contains an additional small Josephson junction and that the shunt capacitance is placed across the junction along with a subset of the array junctions. An analogy can be drawn between δ_L in our circuit and the shunt capacitance in the heavy fluxonium, because they both suppress the qubit transition frequency. Physically, the qubit eigenstates differ when these analogous parameters fall to small values. While the eigenstates collapse to Cooper pair number parity states in our circuit, this is not true for the heavy fluxonium because the variable φ is not compact.

The circuit in Fig. 2a bears resemblance to the rhombus,[47] with two central differences. First, in the rhombus, the superinductances are replaced by single Josephson junctions, or arrays of a few larger junctions.[9,24] This changes the parameter regime of the circuit from $\epsilon_L \ll \epsilon_J$ to $\epsilon_L \sim \epsilon_J$, decreasing the amplitude of the cos 2φ term in the Hamiltonian. Second, the shunt capacitance is replaced by a gate capacitance to a voltage source.[24] This is akin to substituting an electrostatic gate for a shunt capacitance to obtain the Cooper pair box[43] from the transmon;[10] overall

suppression of the charge dispersion is traded for the ability to bias the circuit at its charge sweet spot. Finally, the rhombus by itself is not designed to be a protected qubit. Rather, when multiple rhombi are arranged into a one-dimensional chain (or a two-dimensional fabric), the ground states are eigenstates of a nonlocal operator, which provides topological protection.[9,11,15,45] On one hand, our qubit does not require such scaling to achieve protection. On the other hand, the protection we predict is inherently susceptible to local perturbations (see Relaxation, Pure dephasing).

The 0-π qubit[20] also has a similar superconducting circuit to that in Fig. 2a, but with three essential distinctions. First, the pairs of superinductances on each arm of the circuit are combined, altering the embedding capacitance matrix, in particular the capacitances to ground. Second, there is the addition of a second large capacitance shunting the inductive loop between its two horizontally oriented nodes. When this second capacitance is precisely C_{shunt}, this permits the exact decoupling of the θ mode from the φ mode in Eq. (5). Third, the 0-π qubit is operated in a parameter regime where $\epsilon_L \sim 0.01\epsilon_J$, as opposed to our circuit, where $\epsilon_L \sim 0.1\epsilon_J$.[25] This additional order of magnitude in the superinductance may prove marginally less accessible experimentally.[17,18] Notably, the inductive loop in the 0-π qubit is threaded with $\varphi_{\text{ext}} \approx 0$ at its working point instead of $\varphi_{\text{ext}} = \pi$. This leads to a substantial change in the physics of the ground state manifold; $|0+\rangle$ and $|0-\rangle$ are approximately localized in distinct potential wells.[25] In our case, these states are approximately the symmetric and antisymmetric superpositions of the localized wavefunctions, which are themselves localized in distinct Cooper pair number parities.

Protected qubits face the serious obstacle of realizing state manipulation and measurement while remaining sufficiently isolated from their environments to preserve their coherence. We envision performing readout and control using an ancillary mode structure, which enables cascaded dispersive readout and Raman indirect transitions, as outlined below.

For readout, we aim to exploit the sizable native dispersive shift of the qubit on the plasmon mode, $\chi/2\pi \sim -20$ MHz (see Pure dephasing). Unfortunately, the small anharmonicity, which is at most of order 10 MHz, of the plasmon mode makes readout of the plasmon mode using a linear mode (e.g., a microwave cavity) difficult. As a remedy, we propose introducing an ancillary anharmonic mode by which to measure the plasmon state. In this scheme, a dispersive interaction will be mediated by the ancillary mode between the readout and plasmon modes, thereby enabling dispersive measurement with two readout tones.[48]

The above-mentioned ancillary anharmonic mode will also be useful for control of the protected qubit. As shown earlier, direct transitions mediated by capacitive coupling to the qubit superconducting island are strictly forbidden in the symmetric case, and weakly forbidden in the asymmetric case. Note that this coupling method is chosen to minimize the contributions to decoherence resulting from the introduction of the readout/control circuit. For manipulation, we therefore propose transitioning through the $|1+\rangle$ or $|1-\rangle$ state, as in a conventional Λ system. An additional complication is that, even in the presence of inductive asymmetry, the joint fluxon-plasmon transitions $|0+\rangle \leftrightarrow |1-\rangle$ and $|0-\rangle \leftrightarrow |1+\rangle$ are forbidden.

Using an ancillary mode based on the Superconducting Nonlinear Asymmetric Inductive eLement (SNAIL),[49] it is possible to engineer selection rules where the joint fluxon-plasmon transitions are weakly permitted while the qubit transition is left unaffected, as has recently been demonstrated in a fluxonium qubit.[50] This stems from the feature of the SNAIL that allows, at specific flux biases, third-order nonlinearities without fourth-order nonlinearities. If we parameterize the broken selection rule using $\gamma \in [0, 1)$, the matrix element of $|0+\rangle \leftrightarrow |1-\rangle$ relative to $|0+\rangle \leftrightarrow |1+\rangle$, then the gate speed via sequential direct transitions

and a stimulated Raman transition is estimated to be $(1 + y^{-1})t_{gate}$ and $2\Delta y^{-1}t_{gate}^2$, respectively.[51] Here, $\Delta \sim 100$ MHz is the detuning of the Raman drive from the intermediate state and $t_{gate} \sim 10$ ns is the π-pulse time.[52] This also introduces an additional Purcell loss channel $|0-\rangle \rightarrow |1+\rangle \rightarrow |0+\rangle$ (and vice versa), which corresponds to the relaxation time $T_1 \sim y^{-2}Q_{cap}(\omega_p)/\omega_p$. We therefore expect gate speeds to be slowed by a factor of $y^{-1} < 10$ while lifetimes are kept in the millisecond range.

In summary, we have designed a few-body superconducting circuit in which the charge carriers are well-approximated by pairs of Cooper pairs at a particular bias point. The Josephson tunneling element that supports these charge carriers is characterized by a $\cos 2\varphi$ term in the Hamiltonian, whose emergence we have shown analytically. Our numerical simulations supplement these arguments and demonstrate protection against a variety of common relaxation and dephasing sources. We find that this protection is substantially enhanced in the presence of disorder. Finally, we compared our circuit to similar proposals and offered our perspectives on readout and control.

As a final remark, we comment that engineering a circuit whose potential energy is dominated by a $\cos 2\varphi$ term opens the door to more exotic designs with potential energies of the form $\cos \mu\varphi$, with $\mu \in \mathbb{N}$, which could be obtained by introducing additional loops in the circuit. These could be tremendously valuable for quantum simulation, realizing nearly degenerate ground state manifolds with greater multiplicities, or performing degeneracy-preserving measurements of photon number parity.[53]

DATA AVAILABILITY

Data sharing not applicable to this article as no datasets were generated or analyzed during the current study.

REFERENCES

1. Devoret, M. H. & Schoelkopf, R. J. Superconducting circuits for quantum information: an outlook. *Science* **339**, 1169–1174 (2013).
2. Kelly, J. et al. State preservation by repetitive error detection in a superconducting quantum circuit. *Nature* **519**, 66–69 (2015).
3. Ristè, D. et al. Detecting bit-flip errors in a logical qubit using stabilizer measurements. *Nat. Commun.* **6**, 6983 (2015).
4. Ofek, N. et al. Extending the lifetime of a quantum bit with error correction in superconducting circuits. *Nature* **536**, 441–445 (2016).
5. Murch, K. W. et al. Cavity-assisted quantum bath engineering. *Phys. Rev. Lett.* **109**, 183602 (2012).
6. Shankar, S. et al. Autonomously stabilized entanglement between two superconducting quantum bits. *Nature* **504**, 419–422 (2013).
7. Leghtas, Z. et al. Confining the state of light to a quantum manifold by engineered two-photon loss. *Science* **347**, 853–857 (2015).
8. Puri, S., Boutin, S. & Blais, A. Engineering the quantum states of light in a Kerr-nonlinear resonator by two-photon driving. *NPJ Quantum Inf.* **3**, 18 (2017).
9. Douçot, B. & Ioffe, L. B. Physical implementation of protected qubits. *Rep. Prog. Phys.* **75**, 072001 (2012).
10. Koch, J. et al. Charge-insensitive qubit design derived from the Cooper pair box. *Phys. Rev. A* **76**, 042319 (2007).
11. Douçot, B. & Vidal, J. Pairing of Cooper pairs in a fully frustrated Josephson-junction chain. *Phys. Rev. Lett.* **88**, 227005 (2002).
12. Gladchenko, S. et al. Superconducting nanocircuits for topologically protected qubits. *Nat. Phys.* **5**, 48–53 (2009).
13. Rigetti, C. et al. Superconducting qubit in a waveguide cavity with a coherence time approaching 0.1 ms. *Phys. Rev. B* **86**, 100506 (2012).
14. Wang, Z. et al. Cavity attenuators for superconducting qubits. *Phys. Rev. Appl.* **11**, 014031 (2019).
15. Ioffe, L. B. & Feigel'man, M. V. Possible realization of an ideal quantum computer in Josephson junction array. *Phys. Rev. B* **66**, 224503 (2002).
16. Gottesman, D., Kitaev, A. & Preskill, J. Encoding a qubit in an oscillator. *Phys. Rev. A* **64**, 012310 (2001).
17. Manucharyan, V. E., Koch, J., Glazman, L. I. & Devoret, M. H. Fluxonium: single Cooper-pair circuit free of charge offsets. *Science* **326**, 113–116 (2009).
18. Masluk, N. A., Pop, I. M., Kamal, A., Minev, Z. K. & Devoret, M. H. Microwave characterization of Josephson junction arrays: Implementing a low loss super-inductance. *Phys. Rev. Lett.* **109**, 137002 (2012).
19. Kitaev, A. Protected qubit based on a superconducting current mirror. http://arxiv.org/abs/cond-mat/0609441 (2006).
20. Brooks, P., Kitaev, A. & Preskill, J. Protected gates for superconducting qubits. *Phys. Rev. A* **87**, 052306 (2013).
21. Earnest, N. et al. Realization of a Λ system with metastable states of a capacitively shunted fluxonium. *Phys. Rev. Lett.* **120**, 150504 (2018).
22. Matveev, K. A., Larkin, A. I. & Glazman, L. I. Persistent current in superconducting nanorings. *Phys. Rev. Lett.* **89**, 096802 (2002).
23. Smith, W. C. et al. Quantization of inductively shunted superconducting circuits. *Phys. Rev. B* **94**, 144507 (2016).
24. Bell, M. T., Paramanandam, J., Ioffe, L. B. & Gershenson, M. E. Protected Josephson rhombus chains. *Phys. Rev. Lett.* **112**, 167001 (2014).
25. Dempster, J. M., Fu, B., Ferguson, D. G., Schuster, D. I. & Koch, J. Understanding degenerate ground states of a protected quantum circuit in the presence of disorder. *Phys. Rev. B* **90**, 094518 (2014).
26. Pop, I. M. et al. Coherent suppression of electromagnetic dissipation due to superconducting quasiparticles. *Nature* **508**, 369–372 (2014).
27. Braginsky, V. B., Ilchenko, V. S. & Bagdassarov, K. S. Experimental observation of fundamental microwave absorption in high-quality dielectric crystals. *Phys. Lett. A* **120**, 300–305 (1987).
28. Wang, C. et al. Surface participation and dielectric loss in superconducting qubits. *Appl. Phys. Lett.* **107**, 162601 (2015).
29. Catelani, G., Schoelkopf, R. J., Devoret, M. H. & Glazman, L. I. Relaxation and frequency shifts induced by quasiparticles in superconducting qubits. *Phys. Rev. B* **84**, 064517 (2011).
30. Barends, R. et al. Coherent Josephson qubit suitable for scalable quantum integrated circuits. *Phys. Rev. Lett.* **111**, 080502 (2013).
31. Yan, F. et al. The flux qubit revisited to enhance coherence and reproducibility. *Nat. Commun.* **7**, 12964 (2016).
32. Groszkowski, P. et al. Coherence properties of the 0-π qubit. *New J. Phys.* **20**, 043053 (2018).
33. Cottet, A. *Implementation of a Quantum Bit in a Superconducting Circuit*. Ph.D. Thesis, Université Paris VI (2002).
34. Quintana, C. M. et al. Observation of classical-quantum crossover of $1/f$ flux noise and its paramagnetic temperature dependence. *Phys. Rev. Lett.* **118**, 057702 (2017).
35. Kou, A. et al. Fluxonium-based artificial molecule with a tunable magnetic moment. *Phys. Rev. X* **7**, 031037 (2017).
36. van Harlingen, D. J. et al. Decoherence in Josephson-junction qubits due to critical-current fluctuations. *Phys. Rev. B* **70**, 064517 (2004).
37. Martinis, J. M. et al. Decoherence in Josephson qubits from dielectric loss. *Phys. Rev. Lett.* **95**, 210503 (2005).
38. Houck, A. A. et al. Controlling the spontaneous emission of a superconducting transmon qubit. *Phys. Rev. Lett.* **101**, 080502 (2008).
39. Paik, H. et al. Observation of high coherence in Josephson junction qubits measured in a three-dimensional circuit QED architecture. *Phys. Rev. Lett.* **107**, 240501 (2011).
40. Kumar, P. et al. Origin and reduction of $1/f$ magnetic flux noise in superconducting devices. *Phys. Rev. Appl.* **6**, 041001 (2016).
41. Lin, Y. -H. et al. Demonstration of protection of a superconducting qubit from energy decay. *Phys. Rev. Lett.* **120**, 150503 (2018).
42. van der Wal, C. H. et al. Quantum superposition of macroscopic persistent-current states. *Science* **290**, 773–777 (2000).
43. Vion, D. et al. Manipulating the quantum state of an electrical circuit. *Science* **296**, 886–889 (2002).
44. Steffen, M. et al. High-coherence hybrid superconducting qubit. *Phys. Rev. Lett.* **105**, 100502 (2010).
45. Douçot, B., Feigel'man, M. V. & Ioffe, L. B. Topological order in the insulating Josephson junction array. *Phys. Rev. Lett.* **90**, 107003 (2003).
46. Cottet, A. et al. Implementation of a combined charge-phase quantum bit in a superconducting circuit. *Physica C* **367**, 197–203 (2002).
47. Blatter, G., Geshkenbein, V. B. & Ioffe, L. B. Design aspects of superconducting-phase quantum bits. *Phys. Rev. B* **63**, 174511 (2001).
48. Kirchmair, G. et al. Observation of quantum state collapse and revival due to the single-photon Kerr effect. *Nature* **495**, 205–209 (2013).
49. Frattini, N. E. et al. 3-wave mixing Josephson dipole element. *Appl. Phys. Lett.* **110**, 222603 (2017).
50. Vool, U. et al. Driving forbidden transitions in the fluxonium artificial atom. *Phys. Rev. Appl.* **9**, 054046 (2018).

51. Steck, D. A. *Quantum and Atom Optics* **0.12.6**. http://steck.us/teaching/quantum-optics/quantum-optics-notes.pdf (2019).
52. Chow, J. M. et al. Optimized driving of superconducting artificial atoms for improved single-qubit gates. *Phys. Rev. A* **82**, 040305 (2010).
53. Cohen, J., Smith, W. C., Devoret, M. H. & Mirrahimi, M. Degeneracy-preserving quantum nondemolition measurement of parity-type observables for cat qubits. *Phys. Rev. Lett.* **119**, 060503 (2017).
54. Zorin, A. B. et al. Background charge noise in metallic single-electron tunneling devices. *Phys. Rev. B* **53**, 13682 (1996).

ACKNOWLEDGEMENTS

AUTHOR CONTRIBUTIONS

W.C.S., A.K. and M.H.D. conceived and developed the idea. X.X. contributed to the numerical simulations, and U.V. contributed to the semiclassical analysis. All authors contributed to the manuscript.

COMPETING INTERESTS

The authors declare no competing interests.

ADDITIONAL INFORMATION

Supplementary information is available for this paper at https://doi.org/10.1038/s41534-019-0231-2.

Correspondence and requests for materials should be addressed to W.C.S. or M.H.D.

Reprints and permission information is available at http://www.nature.com/reprints

Publisher's note Springer Nature remains neutral with regard to jurisdictional claims in published maps and institutional affiliations.